npj | 2D materials and applications

Article

Published in partnership with FCT NOVA with the support of E-MRS

https://doi.org/10.1038/s41699-025-00526-8

Charge doping into spin minority states mediates doubling of T_C in ferromagnetic $CrGeTe_3$

Liam Trzaska[1,9], Lei Qiao[2,3,9], Matthew D. Watson[4], Monica Ciomaga Hatnean[5,8], Igor Marković[1,6], Edgar Abarca Morales[1,6], Tommaso Antonelli[1], Cephise Cacho[4], Geetha Balakrishnan[5], Wei Ren[2] ✉, Silvia Picozzi[3,7] ✉ & Phil D. C. King[1] ✉

The recent discovery of the persistence of long-range magnetic order when van der Waals magnets are thinned towards monolayers provides a tunable platform for engineering of novel magnetic structures and devices. Here, we study the evolution of the electronic structure of $CrGeTe_3$ as a function of surface electron doping. From angle-resolved photoemission, we observe spectroscopic fingerprints that this electron doping drives a marked increase in T_C, reaching values more than double that of the undoped material, in agreement with recent studies using electrostatic gating. Together with density functional theory calculations and Monte Carlo simulations, we show that, surprisingly, the increased T_C is mediated by the population of spin-minority Cr t_{2g} states, forming a half-metallic 2D electron gas. This promotes a novel variant of double exchange, and unlocks a significant influence of Ge – which was previously thought to be electronically inert in this system – in mediating Cr-Cr exchange.

Dimensionality has a profound impact on the physical properties of materials. Control of the effective system dimensionality can be used to tune band gaps in semiconductors[1], control catalytic activity[2], and manipulate the strength of electronic interactions[3]. As such, it is of core importance both for fundamental understanding and technological application. This is true no more so than in the field of magnetism. While three-dimensional magnets are commonplace, long-range order is strictly forbidden to occur in one-dimensional systems[4]. Layered materials hosting magnetic ions present a novel environment in which to study the critical dimensionality between these two extremes[5]: finite inter-plane coupling allows long-range order to develop, while the quasi-two-dimensionality of the system can be expected to have a strong influence on the magnetic anisotropy and the role of fluctuations.

Here, we study the quasi-2D layered magnet $CrGeTe_3$. In this compound, magnetic layers are separated by van der Waals gaps, leading to weak inter-layer interactions[6–8]. Nonetheless, recent studies employing electrostatic gating have reported both a dramatic increase in the magnetic ordering temperature, T_C, and a striking switch in the magnetic anisotropy with increasing gate voltage[9], pointing to a subtle interplay between dimensionality and doping effects. We utilise alkali-metal surface doping in ultra-high vacuum to mimic the conditions of field-effect doping, and probe the resulting changes in the surface electronic structure by angle-resolved photoemission spectroscopy (ARPES). Combined with density-functional theory (DFT) calculations, we demonstrate how electrostatic-type doping in this system drives the formation of a half-metallic 2D electron gas of minority-spin carriers, and show how this opens new exchange pathways which underpin the increase in T_C.

Results

Doping-dependent electronic structure of $CrGeTe_3$

Figure 1 shows an overview of the electronic structure of pristine $CrGeTe_3$, and the measured electronic structure following the deposition of sub-monolayer coverage of Rb atoms at the surface. In agreement with our DFT calculations (Fig. 1e), ARPES of the pristine compound (Fig. 1a, b) indicates

[1]SUPA, School of Physics and Astronomy, University of St Andrews, St Andrews, KY16 9SS, UK. [2]Physics Department, International Center of Quantum and Molecular Structures, Materials Genome Institute, State Key Laboratory of Advanced Special Steel, Shanghai Key Laboratory of High Temperature Superconductors, Shanghai University, Shanghai, 200444, China. [3]Consiglio Nazionale delle Ricerche (CNR-SPIN), Unità di Ricerca presso Terzi c/o Università "G. D'Annunzio", 66100 Chieti, Italy. [4]Diamond Light Source, Harwell Science and Innovation Campus, Didcot, OX11 ODE, United Kingdom. [5]Department of Physics, University of Warwick, Coventry, CV4 7AL, United Kingdom. [6]Max Planck Institute for Chemical Physics of Solids, Nöthnitzer Strasse 40, 01187 Dresden, Germany. [7]Department of Materials Science, University of Milan-Bicocca, 20125 Milan, Italy. [8]Present address: Paul Scherrer Institut, Forschungsstrasse 111, 5232 Villigen, PSI, Switzerland. [9]These authors contributed equally: Liam Trzaska, Lei Qiao. ✉e-mail: renwei@shu.edu.cn; silvia.picozzi@spin.cnr.it; pdk6@st-andrews.ac.uk

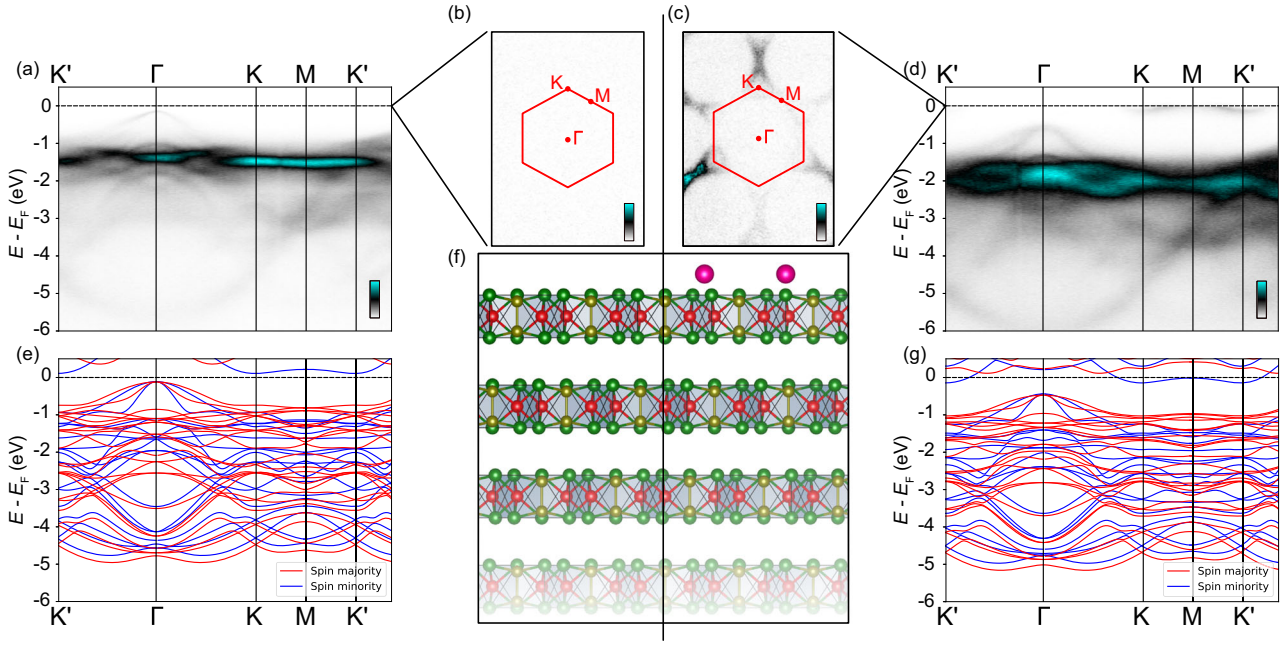

Fig. 1 | Electronic structure of pristine and electron-doped $CrGeTe_3$. a ARPES dispersions measured ($h\nu$ = 80 eV) in the magnetic ground state along the K′ − Γ − K − M − K′ direction of the Brillouin zone for undoped $CrGeTe_3$, reproduced from Ref. 16. **b** Corresponding Fermi surface map. Consistent with the semiconducting nature of $CrGeTe_3$, we find no states at the Fermi level. **c**, **d** Equivalent to (**b**, **a**) for the Rb-doped surface. A clear set of Fermi pockets arises around the K points of the surface Brillouin zone. DFT band structure calculations for (**e**) undoped and (**g**) electron-doped $CrGeTe_3$. **f** Crystal structure of $CrGeTe_3$, showing a schematic of the Rb surface doping.

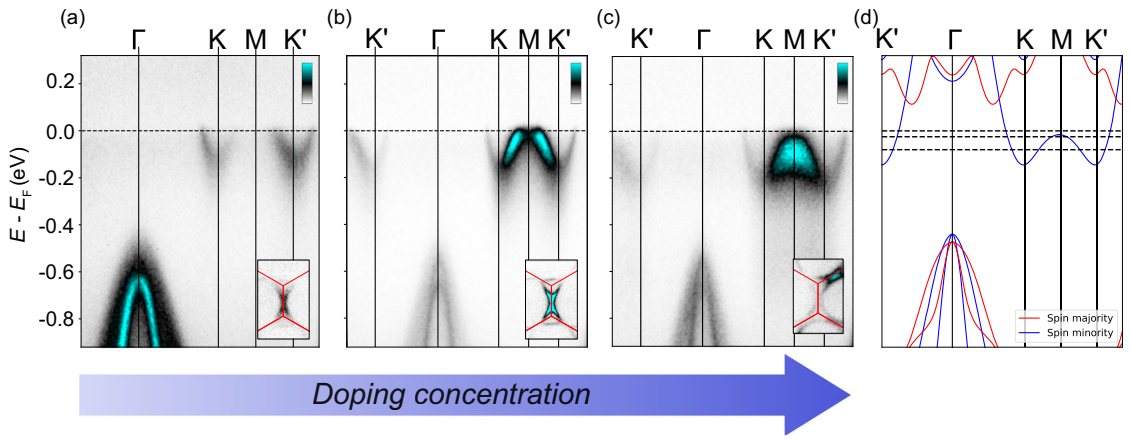

Fig. 2 | Doping-dependent surface Lifshitz transition. a–**c** ARPES dispersions measured along the Γ − K − M − K′ direction of the Brillouin zone for a surface carrier density of (**a**) $N = 3.1 \times 10^{13}$ cm^{-2} ($h\nu$ = 48 eV), (**b**) $N = 4.8 \times 10^{13}$ cm^{-2} ($h\nu$ = 80 eV), and (**c**) $N = 7.9 \times 10^{13}$ cm^{-2} ($h\nu$ = 80 eV). Fermi surface measurements around the M point of the Brillouin zone are shown as insets. The topology of the Fermi surface changes, indicating a doping-dependent Lifshitz transition. **d** DFT calculated band structure, indicating the spin-minority nature of the conduction band. Dashed lines represent E_F for the ARPES measurements shown in (**a**–**c**).

several dispersive states near the top of the valence band, which are dominantly comprised of Te orbital character (see also Supplementary Fig. 1 for orbitally-resolved calculations). These approach, but do not reach, the Fermi level, with negligible spectral weight at E_F consistent with the semiconducting nature of this compound. The rather flat band observed at $E - E_F \approx -1.5\,eV$ is evident in our calculations as the spin-majority Cr-derived states. Consistent with previous calculations[10], we find very little weight of the Ge states in the valence band here (see Supplementary Fig. 1). While Ge is crucial to obtain the chemically stable Cr^{3+} charge state in $CrGeTe_3$, it can be considered as electrically inert in the parent compound.

Upon surface Rb deposition (Fig. 1(d)), the dispersive Te-derived states and the flatter Cr-derived bands are both shifted downwards by around 500 meV (1(d)). This points to an efficient electron doping at the surface, where the deposited Rb atoms become readily ionised, donating their electrons into the near-surface region. We note that similar population of the conduction band has previously been achieved by a similar method via the deposition of K at the surface of $CrGeTe_3$[11]. Consistent with this, we find a finite population of the conduction band states around the K-M-K' path of the surface Brillouin zone. Our measurements indicate the conduction band minimum to be located at the K points (see also Fig. 2), indicating an indirect band gap in this system. Small triangular electron-like Fermi pockets are created around these zone-corner points, clearly visible in our Fermi surface measurements in Fig. 1c. From photon energy-dependent measurements (Supplementary Fig. 2), we find that these states are non-dispersive along the out-of-plane direction, and are thus two-dimensional. We therefore conclude that the alkali metal dosing here leads to a near-surface band bending which, in turn, drives the formation of a 2D electron gas localised at the sample surface[12].

Interestingly, our DFT calculations for an electron-doped $CrGeTe_3$ layer (see Methods) show that the lowest-energy conduction band, which becomes populated upon carrier doping (Fig. 1g), is of spin-minority character. We find a similar conduction band structure in the undoped system (Fig. 1e), a calculation where we manually change the electron density (Fig. 1g) and in supercell calculations where we explicitly include a Rb atom (Supplementary Fig. 3), indicating that this is a robust feature of the electronic structure, intrinsic to $CrGeTe_3$. In fact, previous calculations[13,14] have come to differing conclusions regarding the nature of the lowest conduction band in $CrGeTe_3$. We find that the exact band ordering, and the spin and orbital decomposition of the lowest conduction band is sensitive to the value of the onsite energy U used for the calculations (see Supplementary Fig. 4), explaining the previous variability in calculated electronic structures. We note that only the spin-minority band has the correct momentum-space dispersion to reproduce our experimental measurements, with band minima located at the zone-corner K points. We thus conclude that the low-U regime provides the most accurate calculation scheme for the electron-doped system here, rather than $U = 3$ eV as has been previously reported in the literature. Importantly, the calculations indicate how the low-U ultimately facilitates the formation, on doping, of a two-dimensional half-metal of spin-minority character at the surface here.

Figure 2 shows how this half-metallic 2DEG becomes populated with increasing surface carrier doping. At a surface doping density of 3.1×10^{13} cm^{-2} (0.06 electrons/Cr, Fig. 2a), nearly V-shaped conduction bands are observed centred at the K and K' points of the Brillouin zone, with the conduction band crossing through the Fermi level along the Γ-K and K-M-K' lines. The resulting Fermi surface (Fig. 2a, inset) is comprised of closed triangular pockets centred at the K and K' points. With increasing deposition of Rb on the surface, the conduction band pockets become more occupied, with a concomitant increase in the size of the triangular Fermi pockets (Fig. 2b). At a critical electron doping of around 5×10^{13} cm^{-2} (0.1 electrons/Cr), the Fermi level moves above a saddle point located at the M point of the Brillouin zone (Fig. 2c). This drives a Lifshitz transition[15], where the triangular electron-like Fermi surfaces at low doping merge to form a large hole-like pocket centred at the Brillouin zone centre. These features are well described by our DFT calculations of the electronic structure of a monolayer of $CrGeTe_3$ (Fig. 2d, see Methods, and also Supplementary Fig. 5), indicating that the quantum-confined 2DEG here is well represented within a monolayer description.

Increase of T_C with carrier doping

We now turn to the magnetic order of this surface-doped layer. Previously, some of us have identified a particular state in the valence band of the undoped compound – derived from hybridised Te 5p and Cr e_g states – which shows a strong temperature-dependent shift associated with the development of long-range magnetic order (see Fig. 3c, inset)[16]. This band feature is also evident in our doped samples, for example in Fig. 3a as the bright spectral weight marked by a red arrow at the Γ point at $E - E_F \approx -2.9$ eV. As is evident in the raw data in Fig. 3a, and in energy distribution curves (EDCs) extracted at the Γ point (Fig. 3b), this hybridised state shifts away from the Fermi level with decreasing temperature. We monitor the temperature-dependent separation of this hybridised state from the top of the Te 5p-derived valence bands as a fingerprint of the onset of long-range magnetic order here, where the cross-referencing to the valence band top ensures that temperature-dependent chemical potential shifts or residual sample charging due to the semiconducting bulk cannot affect our conclusions. From this (Fig. 3c), we find that the onset of the shift to higher binding energies of the hybridised state starts at around 120 K for the sample shown here with an electron doping of $N = 3.1 \times 10^{13}$ cm^{-2}, considerably higher than for the undoped bulk where such energy shifts onset at the bulk T_C of ≈ 65 K. We also note that the valence bands are located at slightly higher binding energy for the undoped compound than the doped

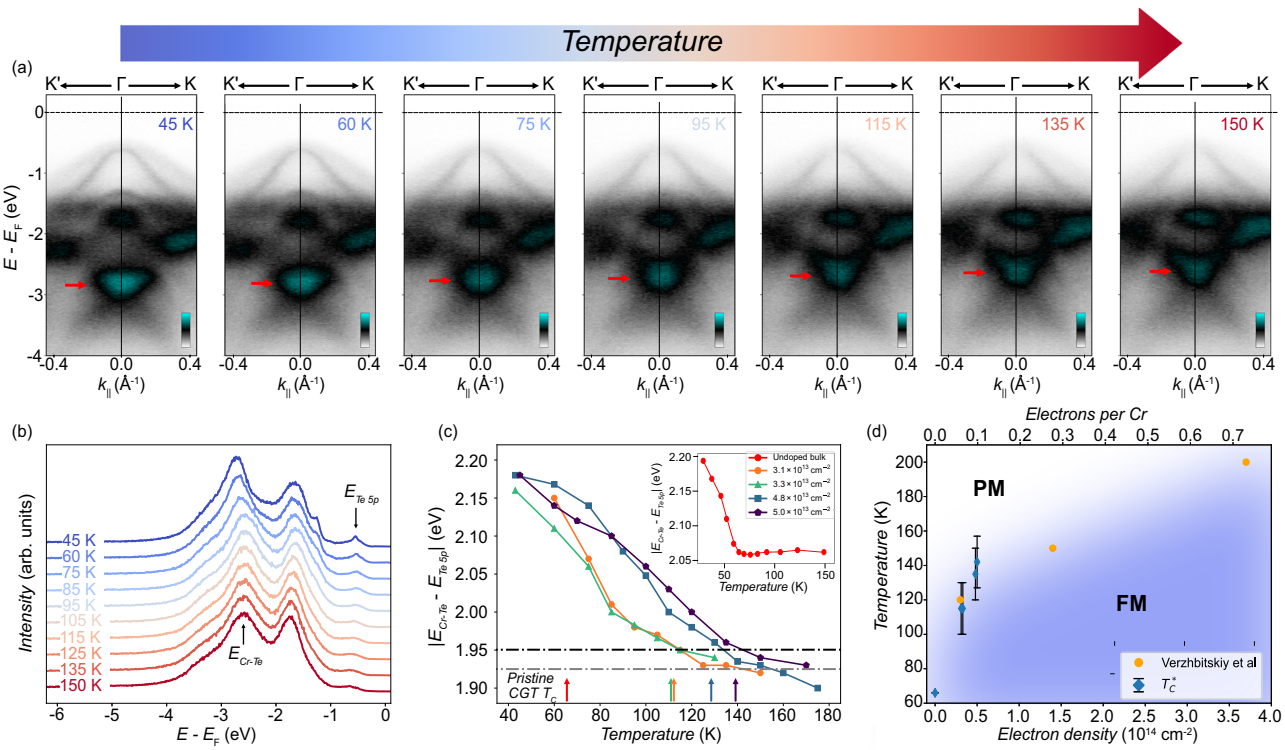

Fig. 3 | Temperature-dependent ARPES measurements. a ARPES measurements around the Γ point ($h\nu = 48eV$) for a $CrGeTe_3$ sample with carrier density $N = 3.1 \times 10^{13}$ cm^{-2}, as a function of temperature, with the relevant states highlighted by red arrows. **b** Corresponding temperature-dependant EDCs extracted at Γ. **c** Extracted temperature-dependent separation of the Cr-Te hybridised state from the Te 5p valence band maximum (see arrows in (**a**) and (**b**)). Grey and black dashed lines represent an estimated baseline and a 10% rise from that baseline. Approximate values for T_C are given by the intersection of each data set with the black dashed line, indicated by the coloured arrows. The magnetic T_C for pristine $CrGeTe_3$ is also shown, and the corresponding temperature-dependent band shifts are shown inset, reproduced from Ref. 16. **d** Experimental phase diagram, plotting the extracted T_C estimates as a function of doping along with estimates from transport measurements from Ref. 9.

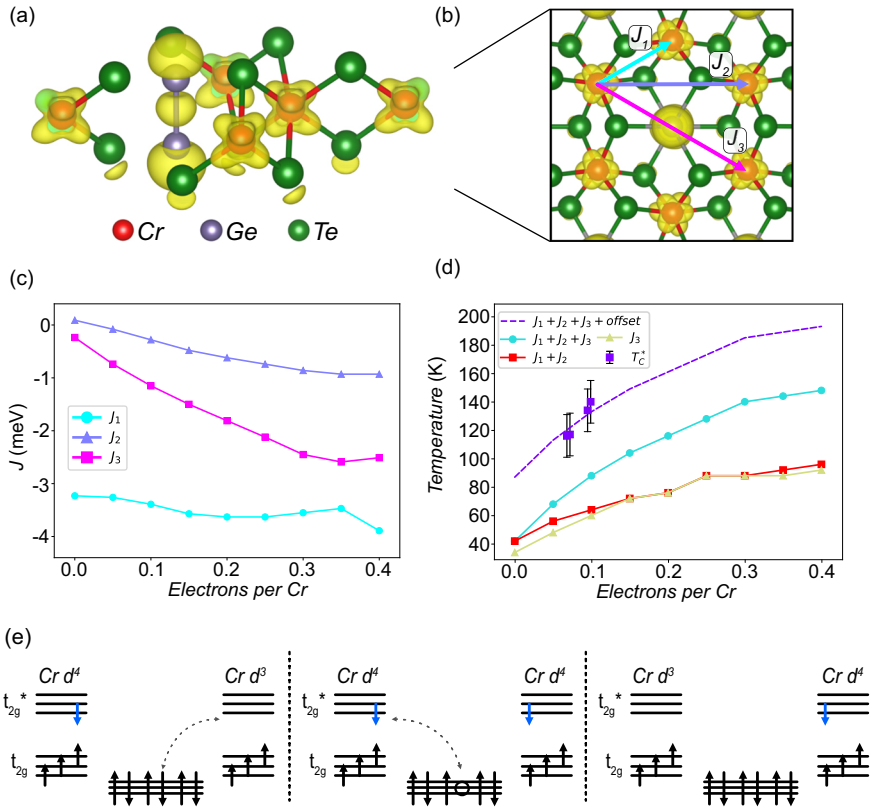

Fig. 4 | Doping-dependent T_C increase. **a** Calculated charge density (yellow surface), integrated over an energy range of 0.2 eV around the spin-minority conduction band minimum and superimposed onto the crystal structure of $CrGeTe_3$ and (**b**) corresponding top-down view of the surface layer. The lobes of the charge density around each Cr site point in between the Cr-Te bond axis, a signature of t_{2g} character, while the charge density around the Ge dimers is dramatically enhanced, pointing to a new conduction path involving the Ge sites. J_1, J_2, and J_3 paths are labeled with colour coded arrows. **c** Calculated values for J_1, J_2, and J_3, plotted as a function of doping concentration. The absolute value of J_3, in particular, shows a dramatic enhancement with doping. **d** T_C extracted from Monte Carlo simulations, considering different combinations of $J_{1,2,3}$, plotted alongside the experimental data. Here, J_3 is required (and has the equivalent impact of J_1 and J_2 combined) to match the shape of the experimental phase diagram. The dashed line through the experimental data points is the calculation for $J_1 + J_2 + J_3$ offset by 45 K, as a guide for the reader in showing the relative trends between experiment and simulation. **e** Schematic representation of the mechanism to enhance T_C enabled by the doped carriers in the minority-spin t_{2g} manifold. Hopping paths from Cr to Te include direct Cr-Te-Cr hopping (J_1), and higher-order paths (J_2) as well as effective Cr-Cr exchange pathways that are mediated via the Ge sites (i.e. J_3).

compound, reflecting a potential role of quantum confinement from the surface doping here for the top-most Te-derived states.

Irrespective, we find that the onset of the energetic shifts of the Cr-Te hybridised state here is systematically moved to higher temperatures with increasing surface doping level (Fig. 3(c)). This indicates that the induced carriers are mediating an increased T_C here, consistent with both studies of the bulk where carriers are generated by organic ion intercalation with tetrabutyl ammonium[17], and with the observation of an enhanced T_C in electrostatically-doped $CrGeTe_3$[9]. While T_C is clearly enhanced for the doped surfaces here, extracting a quantitative measure of T_C is challenging as the transition is not particularly sharp in our measurements, reflecting the complexity of temperature-dependent measurements for an alkali-doped surface. To allow making robust comparisons between the samples, we therefore estimate a baseline of the binding energy at high temperature in our *Evs.T* curves (grey dashed line from Fig. 3c) and determine a T_C value as the temperature at which our measured band shifts cross a threshold at 10% of the total binding energy shift (black dashed line from Fig. 3c). From this, we extract the doping-dependent phase diagram shown in Fig. 3d. We observe a rapid increase in T_C from the bulk value already with our lowest electron doping. T_C then continues increasing with increasing doping density, also in line with the results from electrostatic gating which we include in our phase diagram[9], but with a much slower rate. It thus appears that the introduction of free carriers in the relatively low-doping regime, at and around the point where the spin-minority states are populated and the van Hove singularity in the conduction band is traversed, are the most important for mediating a T_C-enhancement in this system.

Mechanisms of enhanced magnetic order

To explore the origins of this further, we study the evolution of the exchange parameters, J_i, as a function of doping from our DFT calculations, considering up to third-nearest neighbour terms ($i = 3$, Fig. 4a, b). Interestingly, we find modest increases in both the nearest and next-nearest neighbour terms with increasing electron doping, and a rather dramatic increase in J_3 (Fig. 4c). We can understand this from the nature of the conduction band states which become populated upon electron doping. In an octahedral configuration, the naive choice for the next orbital to become occupied upon electron doping would be a spin-majority e_g state. Indeed, there is a significant amount of unoccupied e_g spectral weight peaked at around 0.7 eV above the band gap (see Supplementary Fig. 6), and virtual hopping processes into these states are thought to be relevant for the superexchange in the undoped system[16]. However, our calculated charge density distribution about the Cr sites for the lowest conduction band (Fig. 4a) exhibits lobes pointing between the neighbouring Te sites, indicating a t_{2g}-like character (where we are considering within the octahedral basis, i.e., where the x, y, z axes are oriented along the octahedral axes defined by the Cr-Te bonds). This is consistent with the spin-minority nature of the states at the bottom of the conduction band, as well as a direct projection of its orbital character from our calculations (Supplementary Fig. 6 and Supplementary Fig. 7). This band, however, sits well below the majority of the unoccupied t_{2g} weight[18] (see also Supplementary Fig. 6), and is surprisingly dispersive, dropping below the e_g states at the K and M points. In fact, our calculations reveal a notable charge density of this band also around the Ge sites. This points to a significant hybridisation of the states at the bottom of the conduction band with Ge, which had typically been thought to play a relatively inert role in the magnetic properties of (undoped) $CrGeTe_3$. Considering the J_3 exchange pathway, however, (Fig. 4(b)), it is clear how in the electron-doped system, hopping via the Ge sites could mediate a significant increase in J_3. We note that for doping into the spin-majority e_g-like states, a much more modest involvement of the Ge states can be expected, as evident from our calculated charge density for these states shown in Supplementary Fig. 7.

We show in Fig. 4d an estimate from Monte Carlo calculations (see also Supplementary Fig. 8) of the doping-dependent T_C that would be expected, given such a change in exchange parameters as calculated here. T_C increases monotonically and approximately linearly in the low-doping regime. While modest changes in T_C can be expected for very low dopings, in the doped-semiconductor regime, when the doping becomes sufficient that the system

is metallic, a significant increase in T_C can be expected, consistent with our experimental measurements. Indeed, considering the evolution of all calculated exchange constants (purple line in Fig. 4d), we find that the calculated T_C slightly underestimates the experimental values both for the bulk and the doped systems, but with a doping-dependent trend which closely follows our experimental results (see also offset calculation, purple dashed line in Fig. 4d). Excluding either the increase in J_3 (green line in Fig. 4d) or in J_1 and J_2 (red line in Fig. 4d), it is clear that approximately half of the increase observed here originates from the new hopping pathway which is opened up via the Ge dimers, shown in Fig. 4a and b.

The effect of magnetic anisotropy changes vs doping was included in the spin-Hamiltonian used in the Monte Carlo simulations to estimate the Curie temperature, indicating a doping-dependent magneto-crystalline anisotropy (MCA) which changes sign with increasing carrier density. While the precise doping density at which this occurs will be sensitive to the detailed parameters used in the calculations[19], this general doping-dependent trend is in good agreement with previous calculations[9] (see Methods and Supplementary Fig. 9). However, despite generally being a very important microscopic ingredient in the magnetism of 2D systems[20], in this specific case, the magnetic anisotropy seems not to play a major role. The trend of the T_c (estimated including magnetic anisotropy terms) closely follows that of $J_1 + J_2 + J_3$ isotropic Heisenberg-only terms. Moreover, we performed Monte Carlo calculations where we fix the magnetic exchange parameters as calculated for the undoped system, but change the MCA in accordance with its doping-dependent evolution: as shown in Supplementary Fig. 10, we find no significant change in the predicted T_C.

Discussion

We attribute the resulting increase in T_C here to an unusual form of double exchange, mediated via a dispersive branch of the spin-minority t_{2g} carriers, as summarised schematically in Fig. 4(e). In a simple picture, we can consider the undoped electronic structure of $CrGeTe_3$ as having a half-filled t_{2g} manifold in a d^3 electron configuration. (We note that, in reality, even for the undoped compound, finite mixing with the ligand states plays a crucial role, ultimately underpinning the ferromagnetic order via a superexchange mechanism[16].) The doped carriers must therefore fill either the majority-spin e_g states or the minority-spin t_{2g} states. Our DFT calculations above indicate the latter occurs here at low doping, thus leading to an additional Cr spin on some sites which is anti-aligned with the majority spin moment. Given the dispersive nature of the t_{2g}-derived state at the bottom of the conduction band here, this doped carrier can readily delocalise through the crystal, hopping via the Te sites (including the Cr-Te-Ge-Te-Cr hopping pathway identified above). This, however, requires the creation of a hole on the Te site that has equal spin as the doped electron, which thus acts to mediate a net ferromagnetic coupling here (Fig. 4e).

Since the doped carriers occupy the minority-spin t_{2g} states, the net magnetic moment will be partially cancelled. Indeed, as shown in Supplementary Fig. 11, we find that the magnetic moment decreases linearly with the increase of doping concentration at low doping levels. As the doping concentration increases further, however, the spin-majority e_g states start to become populated (Fig. 2d), resulting in fluctuations in the magnetic moment (Supplementary Fig. 11). Consistent with this, we find that the increase in J and the associated increase in calculated T_C starts to saturate above a critical doping of around 0.3 electrons/Cr (Fig. 4c, d). These trends are in good agreement with experiments (Fig. 3d), validating our DFT approach. It will be an interesting subject for further study to consider whether beyond-DFT methods can obtain even better quantitative accuracy with our measurements. Already here, our study highlights how the population of spin-minority conduction band states with electron doping in $CrGeTe_3$ mediates a more than doubling of its ferromagnetic T_C, explaining recent findings of gate-tuned magnetism in this system. Our findings also highlight an unusual situation that occurs here under such electrostatic doping, with a half-metal forming at the surface which has opposite spin-polarisation to the bulk, thus suggesting potential for novel spintronic devices such as intrinsic, and gate-tunable, spin valve structures, magnetic tunnel junctions, or spin-filters[21].

Methods

Sample growth

$CrGeTe_3$ single crystals were prepared following the procedure in Ref. 7. The crystals were separated from the flux by centrifuging at 500°C and then cleaned of any excess Te. The crystals were found to exhibit a sharp magnetic transition at approximately 65 K[16], in good agreement with previous literature reports for pristine bulk $CrGeTe_3$[8].

Angle-resolved photoemission spectroscopy

ARPES measurements were performed at the high-resolution branch of the I05 beamline at Diamond Light Source, UK. Bulk single crystal samples were cleaved in situ after being cooled to approximately 40 K, and then electron-doped by depositing Rb atoms on the surface via evaporation from a SAES getter source. To obtain variable electron density, the samples were dosed for varying time, between 30 s and 360 s. The chamber pressure did not exceed 7×10^{-10} mbar during the deposition. The alkali surface doping leads to an increase in carrier concentration only close to the surface, with a spatial extent governed by the Thomas-Fermi screening length, and an associated near-surface band bending. We find that the doped surface layer is in reasonable approximation to a monolayer-like system. Note, we would expect qualitatively similar findings as presented in the main text if other alkali metals were used, with the primary role of the alkali metal being to electron dope into the near-surface region.

ARPES measurements were performed using linearly polarised photons (with photon energies as specified in the figure captions) at sample temperatures ranging between 40 K and 200 K. Since $CrGeTe_3$ is a semiconductor, sample charging due to photoemission can become problematic at low temperatures[22]. To minimise the impact of this, we limited our measurement range to above 40 K and used rather low photon fluxes. To further rule out any influence of sample charging on our conclusions, we extract T_C based on analysis of energy differences in our measured spectra, as outlined in the text.

The doping levels were estimated from our measured ARPES data using Luttinger's Theorem[23], where the volume enclosed by the Fermi surface is proportional to the particle density by,

$$N = g \int \frac{d^D k}{(2\pi)^D}, \quad (1)$$

where N is the number of charge carriers, D is the dimensionality of the system, and g is the spin and valley degeneracy, characterising how many equivalent bands exist within the first Brillouin zone, with $D = 2$ here. The area enclosed by the Fermi surface was extracted from our fitted Fermi surface data by implementing a Green's Theorem algorithm.

Density functional theory and Monte Carlo calculations

Our calculations were carried out within the Perdew-Burke-Ernzerhof (PBE) generalized gradient approximation[24], a commonly-used approximation to treat the exchange-correlation potential term within DFT, here as implemented in the Vienna *ab* Initio Simulation Package (VASP)[25]. To better consider the vdW forces, we performed calculations with a non-local vdW density functional in the form of optB86b-vdW[26,27]. The interactions of electrons with ionic cores were described using projector-augmented wave (PAW) pseudopotentials[28,29]. For all the calculations, we chose the energy cutoff to be 600 eV, the maximum force of all atoms was optimized until it fell to less than 0.01 eV/Å, and the criterion for the total energy convergence was set as 10^{-6} eV. The set of $12 \times 12 \times 1$ *k*-point samplings[30], in the reciprocal space by the Gamma-centered grid, was used to model the Brillouin zone. A vacuum space exceeding 20 Å was included to avoid interaction between adjacent periodic layers for the monolayer calculations.

In this work, all of the geometry structures were fully relaxed, according to the maximum force and total energy convergence, listed previously. The lattice constant a and b of optimized monolayer $CrGeTe_3$ are 6.90 Å, which is close to 6.91 Å reported by Fang et al.[31]. We calculated the energy of different dopant positions and found that the configuration in which the Rb is located directly above the Cr sites has the lowest energy (Supplementary Fig. 12). This superstructure was then used to calculate the band structure. Our calculations indicated that the effects of electron doping are dominated by a rigid shift of the band structure. For the calculation of the exchange parameters and magnetic moments as a function of electron doping, we thus artificially changed the number of electrons to simulate the non-integer doping concentration. This allows us to calculate a continuously varying doping concentration, including the regime of low doping levels, which would be unfeasible for direct supercell calculations with chemical doping. We have validated this approach against supercell calculations for high carrier densities, where the supercell with chemical dopants becomes of a feasible size. Throughout, we refer to the supercell calculations as Rb-doped in the caption, while the DFT results calculated by artificially changing the electron number are referred to as electron-doped. We note that these doping calculations were performed without spin-orbit coupling. Whilst spin-orbit coupling leads to significant changes for the Te-derived valence bands[16] see Supplementary Fig. 13, we confirmed that they have minimal impact on the conduction band electronic structure and on the calculated exchange parameters, as shown in Supplementary Fig. 14.

We used the VAMPIRE[32] code to perform Monte Carlo (MC) simulations. The magnetic properties can be modelled via the following spin Hamiltonian for classical spins:

$$H = \frac{1}{2}\sum_{ij} J_{ij} S_i \cdot S_j + \sum_i A_i \cdot S_i^2, \tag{2}$$

assuming isotropic exchange constants up to the third nearest neighbour. Anisotropic effects were modelled via an effective magneto-crystalline anisotropy (MCA) term, with coupling constant A_i, obtained upon including spin-orbit coupling in the DFT calculations. The J terms were extracted by the energy mapping method[33], with a negative value indicating ferromagnetic interactions. The energy mapping method is a method to solve the magnetic exchange parameters within a Heisenberg model by combining the energies of the magnetic configurations. Here we calculated the energy of the four configurations shown in Supplementary Fig. 15 through DFT, and substituted them into the left side of the energy expression shown. Then one can obtain $J_1 - J_3$ by combining the four equations. The unit cell we use is rectangular, which is consistent with periodic boundary conditions of the honeycomb lattice and is able to host - within the same unit cell - four different spin configurations. The standard Metropolis algorithm[34] has been used for MC simulations with 5×10^4 MC steps for equilibration and 3×10^5 MC steps for averaging. Since the VAMPIRE software can only simulate cuboid cells, we used cuboid cells, which contain 4 Cr sites. We performed calculations for a $40 \times 40 \times 1$ supercell with $N_s = 6400$ spins. The transition temperature can be estimated from the peaks that appear in the temperature evolution of specific heat (Supplementary Fig. 8), evaluated as:

$$C_v = \frac{k_B \beta^2}{N_s}[\langle E^2 \rangle - \langle E \rangle^2] \tag{3}$$

where E is the energy calculated using VAMPIRE, k_B is the Boltzmann constant and $\beta = 1/k_B T$, while $\langle \ldots \rangle$ indicates statistical averages.

Data availability

The research data supporting this publication can be accessed at https://doi.org/10.17630/d2994e11-d310-46f1-9fa3-927d9895443f[35].

Received: 19 June 2024; Accepted: 7 January 2025;
Published online: 17 January 2025

References

1. Chaves, A. et al. Bandgap engineering of two-dimensional semiconductor materials. *npj 2D Mater. Appl.* **4**, 29 (2020).
2. Cao, C. et al. Dimensionality control of electrocatalytic activity in perovskite nickelates. *Nano Lett.* **20**, 2837–2842 (2020).
3. King, P. D. C. et al. Atomic-scale control of competing electronic phases in ultrathin $LaNiO_3$. *Nat. Nano* **9**, 443–447 (2014).
4. Peierls, R. On Ising's model of ferromagnetism. *Math. Proc. Camb. Philos. Soc.* **32**, 477–481 (1936).
5. Gibertini, M., Koperski, M., Morpurgo, A. F. & Novoselov, K. S. Magnetic 2D materials and heterostructures. *Nat. Nanotechnol.* **14**, 408–419 (2019).
6. Carteaux, V., Brunet, D., Ouvrard, G. & Andre, G. Crystallographic, magnetic and electronic structures of a new layered ferromagnetic compound $Cr_2Ge_2Te_6$. *J. Phys.: Condens. Matter* **7**, 69 (1995).
7. Ji, H. et al. A ferromagnetic insulating substrate for the epitaxial growth of topological insulators. *J. Appl. Phys.* **114**, 114907 (2013).
8. Liu, Y. & Petrovic, C. Critical behavior of quasi-two-dimensional semiconducting ferromagnet $Cr_2Ge_2Te_6$. *Phys. Rev. B* **96**, 054406 (2017).
9. Verzhbitskiy, I. A. et al. Controlling the magnetic anisotropy in $Cr_2Ge_2Te_6$ by electrostatic gating. *Nat. Electron.* **3**, 460–465 (2020).
10. Wang, K., Nikolaev, S., Ren, W. & Solovyev, I. Giant contribution of the ligand states to the magnetic properties of the $Cr_2Ge_2Te_6$ monolayer. *Phys. Chem. Chem. Phys.* **21**, 9597–9604 (2019).
11. Li, Y. F. et al. Electronic structure of ferromagnetic semiconductor $CrGeTe_3$ by angle-resolved photoemission spectroscopy. *Phys. Rev. B* **98**, 125–127 (2018).
12. Riley, J. M. et al. Negative electronic compressibility and tunable spin splitting in WSe_2. *Nat. Nanotechnol.* **10**, 1043–1047 (2015).
13. Liu, L. et al. Tunable electronic properties and enhanced ferromagnetism in $Cr_2Ge_2Te_6$ monolayer by strain engineering. *Nanotechnology* **32**, 485408 (2021).
14. Wang, K. et al. Magnetic and electronic properties of $Cr_2Ge_2Te_6$ monolayer by strain and electric-field engineering. *Appl. Phys. Lett.* **114**, 092405 (2019).
15. Lifshitz, I. M. Anomalies of electron characteristics in the high pressure region.*Zhur. Eksptl'. i Teoret. Fiz.* **38**, https://www.osti.gov/biblio/4173345 (1960).
16. Watson, M. D. et al. Direct observation of the energy gain underpinning ferromagnetic superexchange in the electronic structure of $CrGeTe_3$. *Phys. Rev. B* **101**, 205125 (2020).
17. Wang, N. et al. Transition from ferromagnetic semiconductor to ferromagnetic metal with enhanced curie temperature in $Cr_2Ge_2Te_6$ via organic ion intercalation. *J. Am. Chem. Soc.* **141**, 17166–17173 (2019).
18. Kang, S., Kang, S. & Yu, J. Effect of coulomb interactions on the electronic and magnetic properties of two-dimensional $CrSiTe_3$ and $CrGeTe_3$ materials. *J. Electron. Mater.* **48**, 1441–1445 (2019).
19. Haddadi, F., Linscott, E., Timrov, I., Marzari, N. & Gibertini, M. On-site and intersite hubbard corrections in magnetic monolayers: The case of $feps_3$ and cri_3. *Phys. Rev. Mater.* **8**, 014007 (2024).
20. Torelli, D. et al. High throughput computational screening for 2D ferromagnetic materials: the critical role of anisotropy and local correlations. *2D Mater.* **6**, 045018 (2019).
21. Tang, Q. & Zhu, X. Half-metallic double perovskite oxides: recent developments and future perspectives. *J. Mater. Chem. C.* **10**, 15301–15338 (2022).
22. Baer, D. R. et al. XPS guide: Charge neutralization and binding energy referencing for insulating samples. *J. Vac. Sci. Technol. A* **38**, 031204 (2020).
23. Luttinger, J. M. & Ward, J. C. Ground-state energy of a many-fermion system. ii. *Phys. Rev.* **118**, 1417–1427 (1960).
24. Perdew, J. P., Burke, K. & Ernzerhof, M. Generalized gradient approximation made simple. *Phys. Rev. Lett.* **77**, 3865 (1996).
25. Kresse, G. & Hafner, J. Ab initio molecular dynamics for liquid metals. *Phys. Rev. B* **47**, 558 (1993).

26. Klime, J., Bowler, D. R. & Michaelides, A. Van der Waals density functionals applied to solids. *Phys. Rev. B* **83**, 195131 (2011).
27. Klimeš, J., Bowler, D. R. & Michaelides, A. Chemical accuracy for the van der Waals density functional. *J. Phys.: Condens. Matter* **22**, 022201 (2009).
28. Blöchl, P. E. Projector augmented-wave method. *Phys. Rev. B* **50**, 17953 (1994).
29. Kresse, G. & Joubert, D. From ultrasoft pseudopotentials to the projector augmented-wave method. *Phys. Rev. B* **59**, 1758 (1999).
30. Monkhorst, H. J. & Pack, J. D. Special points for Brillouin-zone integrations. *Phys. Rev. B* **13**, 5188 (1976).
31. Fang, Y., Wu, S., Zhu, Z.-Z. & Guo, G.-Y. Large magneto-optical effects and magnetic anisotropy energy in two-dimensional $Cr_2Ge_2Te_6$. *Phys. Rev. B* **98**, 125416 (2018).
32. Evans, R. F. et al. Atomistic spin model simulations of magnetic nanomaterials. *J. Phys.: Condens. Matter* **26**, 103202 (2014).
33. Xiang, H., Lee, C., Koo, H.-J., Gong, X. & Whangbo, M.-H. Magnetic properties and energy-mapping analysis. *Dalton Trans.* **42**, 823–853 (2013).
34. Asselin, P. et al. Constrained Monte Carlo method and calculation of the temperature dependence of magnetic anisotropy. *Phys. Rev. B* **82**, 054415 (2010).
35. Trzaska, L. et al. Charge doping into spin minority states mediates doubling of T_C in ferromagnetic $CrGeTe_3$ (dataset). Dataset. University of St Andrews Research Portal. https://doi.org/10.17630/d2994e11-d310-46f1-9fa3-927d9895443f (2025).

Acknowledgements

We thank Philip Murgatroyd, Bernd Braunecker, and Chris Hooley for useful discussions. We gratefully acknowledge support from The Leverhulme Trust via Grant No. RL-2016-006, and the UK Engineering and Physical Sciences Research Council via Grant Nos. EP/X015556/1, EP/T005963/1, and EP/N032128/1. P.K. and S.P. acknowledge support from the Royal Society through the International Exchange grant IEC\R2\222041. IM and EAM gratefully acknowledge studentship support from the International Max-Planck Research School for Chemistry and Physics of Quantum Materials. We thank Diamond Light Source for access to Beamline I05 (Proposals SI21986 and SI25564), which contributed to the results presented here. S.P. acknowledges support from the Ministry of University and Research (MUR) PRIN 2022 project "SORBET - Spin ORBit Effects in Two-dimensional magnets", project No. 2022ZY8HJY. L.Q. acknowledges the support from China Scholarship Council, W.R. acknowledges the support from the National Natural Science Foundation of China (12074241, 11929401, 52130204), and the Science and Technology Commission of Shanghai Municipality (22XD1400900, 20501130600). For the purpose of open access, the authors have applied a Creative Commons Attribution (CC BY) licence to any Author Accepted Manuscript version arising.

Author contributions

LT, MDW, IM, EAM, TA, and PDCK measured the ARPES data, which was analysed by LT. LQ and SP performed the DFT calculations. MCH and GB grew and characterised the samples. MDW and CC maintained the ARPES endstation and provided experimental support. LT, LQ, SP, and PDCK wrote the manuscript, with input and discussions from all co-authors. WR, SP, and PDCK oversaw the project.

Competing interests

The authors declare no competing interests.

Additional information

Supplementary information The online version contains supplementary material available at https://doi.org/10.1038/s41699-025-00526-8.

Correspondence and requests for materials should be addressed to Wei Ren, Silvia Picozzi or Phil D. C. King.